16. D. S. Scheirer and K. C. Macdonald, *ibid.* **98**, 7871 (1993).
17. MBAs are calculated by subtracting from the free-air anomaly the gravitational attraction of sea-floor topography and Moho relief that is assumed to parallel the sea floor (except that the Moho does not shoal beneath seamounts). If crust has a constant density and thickness and the mantle density is constant, then the MBA will be constant.
18. R. S. Detrick *et al.*, *Science* **259**, 499 (1993).
19. J. C. Mutter *et al.*, *ibid.* **268**, 391 (1995).
20. S. A. Hussenoeder *et al.*, *J. Geophys. Res.* **101**, 22087 (1996).
21. J. J. Mahoney *et al.*, *Earth Planet. Sci. Lett.* **121**, 173 (1994).
22. W. Bach, E. Hegner, J. Erzinger, M. Satir, *Contrib. Miner. Petrol.* **116**, 365 (1994).
23. J. R. Cochran, *Geophys. J. R. Astron. Soc.* **87**, 421 (1986).
24. M.-H. Cormier, K. C. Macdonald, D. S. Wilson, *J. Geophys. Res.* **99**, 8063 (1995).
25. M. K. McNutt and A. V. Judge, *Science* **248**, 969 (1990).
26. J. Phipps Morgan, W. J. Morgan, Y.-S. Zhang, W. H. F. Smith, *J. Geophys. Res.* **100**, 12753 (1995).
27. L. S. Hall and J. M. Sinton, *Eos* **77**, 660 (1996).
28. J.-G. Schilling, D. Fontignie, R. Kingsley, in *Mantle Flow and Melt Generation Beneath Mid-Ocean Ridges, Program with Abstracts* (RIDGE, Providence, RI, 1997); Hall *et al.*, *Eos* **77**, 660 (1996).
29. J. P. Canales, R. S. Detrick, S. Bazin, A. J. Harding, J. A. Orcutt, *Science* **280**, 1218 (1998).
30. S. Bazin *et al.*, *Geophys. Res. Lett.*, in press.
31. D. S. Scheirer, K. C. Macdonald, D. W. Forsyth, Y. Shen, *Mar. Geophys. Res.* **18**, 13 (1996).
32. Y. Shen, D. W. Forsyth, D. S. Scheirer, K. C. Macdonald, *J. Geophys. Res.* **98**, 17875 (1993).
33. E. E. Davis and J. L. Karsten, *Earth Planet. Sci. Lett.* **79**, 385 (1986).
34. R. Batiza and D. Vanko, *J. Geophys. Res.* **89**, 11260 (1984).
35. Y. Niu and R. Batiza, *ibid.* **96**, 21753 (1991).
36. The large, recently active seamounts in the westernmost part of the study area (Fig. 1) are probably created by a mechanism that is distinct from the normal upwelling associated with the EPR, such as small-scale convection or local stretching of the Pacific Plate.
37. E. E. E. Hooft, R. S. Detrick, G. M. Kent, *J. Geophys. Res.* **102**, 27319 (1997).
38. We thank R. Batiza, an anonymous reviewer, and the other MELT investigators for comments that improved this paper. Supported by NSF grants OCE-9402375 and OCE-9615204.

18 February 1998; accepted 21 April 1998

Mantle Seismic Structure Beneath the MELT Region of the East Pacific Rise from *P* and *S* Wave Tomography

Douglas R. Toomey,* William S. D. Wilcock, Sean C. Solomon, William C. Hammond, John A. Orcutt

Relative travel time delays of teleseismic *P* and *S* waves, recorded during the Mantle Electromagnetic and Tomography (MELT) Experiment, have been inverted tomographically for upper-mantle structure beneath the southern East Pacific Rise. A broad zone of low seismic velocities extends beneath the rise to depths of about 200 kilometers and is centered to the west of the spreading center. The magnitudes of the *P* and *S* wave anomalies require the presence of retained mantle melt; the melt fraction near the rise exceeds the fraction 300 kilometers off axis by as little as 1%. Seismic anisotropy, induced by mantle flow, is evident in the *P* wave delays at near-vertical incidence and is consistent with a half-width of mantle upwelling of about 100 km.

Competing models for mantle flow and for the generation and transport of melt beneath mid-ocean ridges (*1*) predict detectable differences in mantle seismic structure. The travel times of body waves from distant earthquakes, recorded by an ocean-bottom array of sensors, should be sensitive to the distribution of melt retained in the mantle and to seismic anisotropy produced by flow-induced finite strain (*2*). Here, we report an analysis of body-wave travel time delays from the MELT Experiment (*3*) on the southern East Pacific Rise (EPR) and their implications for the seismic structure and mantle flow pattern beneath a fast-spreading oceanic ridge.

From a subset of the MELT network (*3*), we measured 500 relative delay times of filtered *P* and *S* waves from 20 earthquakes at epicentral distances greater than 30°. *P* waves were easily identified on the vertical seismometer at frequencies between 0.14 and 0.5 Hz, equivalent to an average seismic wavelength in the mantle of about 35 km (*4*). Shear waves were also observed on horizontal seismometers with good signal-to-noise ratios at frequencies of 0.05 to 0.1 Hz (average upper-mantle seismic wavelength of about 70 km). Because shear wave splitting is observed (*5*), *S* waves polarized in the fast (S_{fast}) and slow (S_{slow}) directions, respectively subparallel and subperpendicular to the spreading direction, were analyzed independently (*6*). For both types of body waves, arrivals are coherent at nearby stations, allowing us to use cross-correlation methods (*7*) to improve the accuracy of estimated delay times (*8*). All delays, measured relative to a standard Earth model (*9*), have had a mean value removed for each event.

Mean *P*-wave delay times in the frequency band 0.14 to 0.5 Hz vary by ~0.7 s across the network; the greatest delays are on and near the rise axis (Fig. 1A). Along the primary ocean bottom seismometer (OBS) array (*3*), the cross-axis delay time pattern is asymmetric. At similar crustal ages, delays to the west are consistently greater by 0.1 to 0.2 s than those to the east; this asymmetry is evident within 5 to 10 km of the rise axis. The cross-axis pattern is not well constrained along the secondary OBS

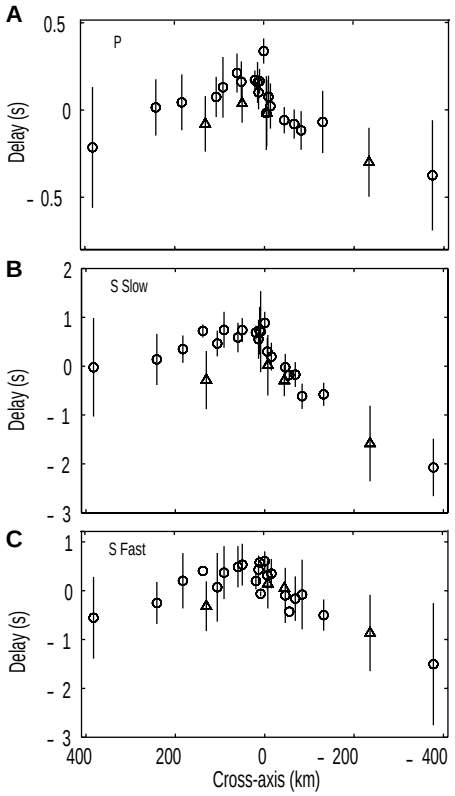

Fig. 1. Mean *P* and *S* wave delays versus cross-axis distance. Circles and triangles denote sites along the primary and secondary OBS arrays (*3*), respectively. Vertical bars indicate standard deviations in observed delays at a given site; uncertainties in individual delays are considerably smaller, ~0.1 s for *P* and 0.3 s for *S*. (**A**) *P* delay; (**B**) S_{slow} delay; (**C**) S_{fast} delay. The S_{slow} and S_{fast} directions, defined by the shear wave splitting analysis (*5*), are approximately subparallel to the rise and spreading directions, respectively.

D. R. Toomey and W. C. Hammond, Department of Geological Sciences, University of Oregon, Eugene, OR 97403, USA.
W. S. D. Wilcock, School of Oceanography, University of Washington, Seattle, WA 98195, USA.
S. C. Solomon, Department of Terrestrial Magnetism, Carnegie Institution of Washington, Washington, DC 20015, USA.
J. A. Orcutt, Institute of Geophysics and Planetary Physics, Scripps Institution of Oceanography, University of California at San Diego, La Jolla, CA 92093, USA.

*To whom correspondence should be addressed. E-mail: drt@newberry.uoregon.edu

array (*3*) because of the fewer stations. Compared with the primary array, arrivals on the western flank of the rise are generally earlier on the secondary array, along which the sea floor is deeper at a given crustal age. On the eastern flank, in contrast, average *P* delays are comparable on the two arrays.

Mean delays for S_{slow} and S_{fast} vary across the network by 2 to 3 s. As for the *P* wave delays, the *S* wave delays are greater on and near the axis and where the sea floor is shallower (Fig. 1, B and C). The cross-axis pattern of delays for S_{slow} (polarized along the rise) is comparable in form to that observed for *P*, though the magnitudes of the *S* delays are larger. For similar crustal ages, delays for S_{slow} to the west of the rise are consistently greater than those to the east by ~0.5 to 2 s. Similar to the pattern for *P* wave delays, this asymmetry in delay is evident within 5 to 10 km of the rise axis and increases with crustal age. The cross-axis pattern of delays for S_{fast} waves (polarized in the spreading direction) is notably different from that for *P* or S_{slow} waves, in that the degree of asymmetry with crustal age is less. Immediately adjacent to the rise, delays for S_{fast} are comparable to the east and west, whereas for S_{slow} the delays to the west are greater, by ~0.5 s, than those to the east. With increasing distance from the rise axis, an asymmetry in S_{fast} becomes evident; the delay at the western end of the array is ~1 s greater than at the eastern end.

At horizontal length scales of several tens to hundreds of kilometers, *P* and *S* delay time patterns are consistent with a low-velocity anomaly that is progressively more pronounced nearer the rise axis and where the rise is shallower, and that decreases in magnitude less rapidly with age beneath the Pacific Plate than beneath the Nazca Plate. At shorter length scales, within 50 km of the rise, *P* and S_{slow} delays are notably asymmetric and display near-axis trends that appear discontinuous about the spreading center; a similar degree of asymmetry is not observed for S_{fast} delays. For each component the mean delay of the axial station is observed to be greatest, which suggests that the vertically averaged velocities are lowest directly beneath the rise.

We inverted a total of 175 *P*, 154 S_{slow}, and 171 S_{fast} delays measured along the primary OBS array to determine independently the two-dimensional velocity structure in a plane perpendicular to the ridge, using a nonlinear method (*10*). As a first approximation, we inverted the data under the assumption that the structure is isotropic. We limited the inverse problem to two-dimensional solutions that were smoothed to give preference to long-wavelength (50 km and greater) variations in structure and heavily damped at depths greater than a squeezing depth (*11*). The squeezing depth Z_s, which varied between 0 and 600 km beneath the sea floor, was used to test the hypothesis that models with lateral heterogeneity confined to depths shallower than Z_s are consistent with the delay time data.

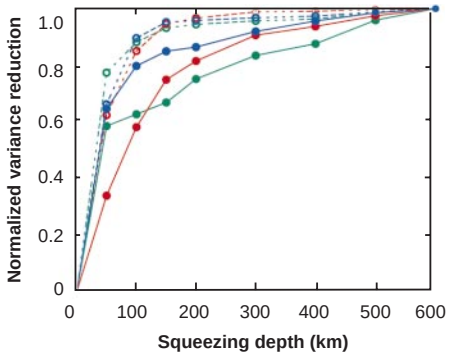

Fig. 3. Normalized variance reduction versus squeezing depth Z_s for inversions of observed (solid curves) and synthetic (dashed curves) data. Curves for *P*, S_{slow}, and S_{fast} are shown in green, blue, and red, respectively.

Independent of the squeezing depth, the results (Fig. 2) consistently show that the most pronounced low-velocity anomaly is less than 200 km beneath the sea floor and that its center is offset by about 20 to 40 km to the west of the rise axis. Plots of normalized variance reduction versus squeezing depth (Fig. 3) show that the fits to the data systematically improve for larger Z_s. A component of this improvement in fit may be attributed to modeling noisy data, because an increase in Z_s also increases the degrees of freedom in the inversion.

To understand further the sensitivity of

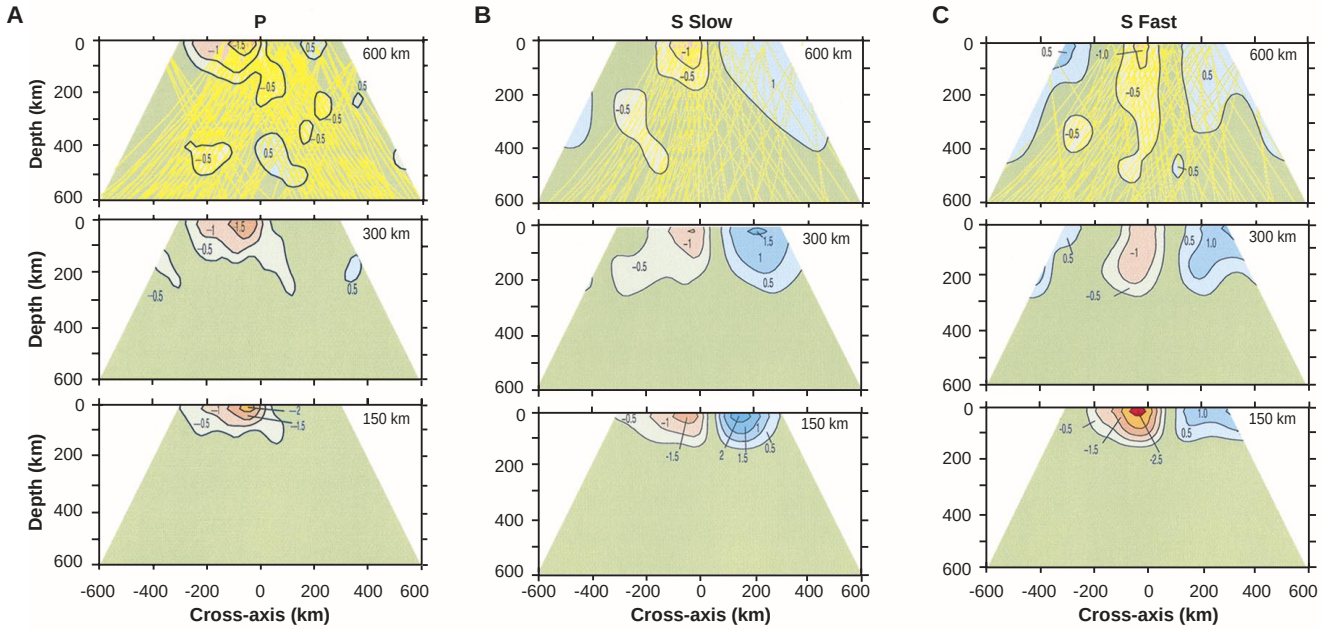

Fig. 2. Results of tomographic imaging contoured in percent deviation from a radial Earth model (*9*); the delay time observations do not constrain absolute velocities, so only relative variations are meaningful. Contour interval is 0.5%; zero contour not shown. Cross-axis direction is positive to the east. (**A**) *P* image; (**B**) S_{slow} image; (**C**) S_{fast} image. Percent deviations more negative than −0.5% and greater than 0.5% are shown by red and blue shades, respectively. Projections onto the section of wave paths used are shown in the top panel for each wave type. The squeezing depth Z_s is indicated for each panel; see text for details.

the variance reduction to Z_s, we conducted a series of inversions for synthetic data calculated from a known velocity model, characterized by a triangular anomaly (velocity 5% less than normal) centered on the rise axis and extending from the surface to 140 km depth (*12*). The results (dashed curves in Fig. 3) yield a relation between variance reduction and Z_s that exhibits significantly more curvature than that of the actual data. For the synthetic data, when Z_s is greater than the depth extent of the input anomalous structure (140 km), the average slope of the variance reduction curve is approximately zero. Comparison of the variance reduction curves for the synthetic and observed data suggests that the gradual improvement in variance reduction with increasing Z_s for the observed delays is consistent with the presence of anomalous structures at depths as great as 200 to 300 km. For this reason, we prefer tomographic results obtained with a squeezing depth of 300 km; the maximum depth of the anomalous structure is uncertain.

The low velocities revealed by tomographic imaging and the progressive increase in *P* and *S* delay times toward the rise cannot be fully explained by expected temperature variations beneath the spreading center. The lateral variations in seismic velocity contributed by the cooling of oceanic lithosphere, including the effects of anelastic dispersion (*13*), yield near-axis delays that are 0.1 and 0.4 s greater than at 400 km off axis for *P* and *S* waves, respectively. These predicted variations are considerably smaller than the observed increase in delays toward the rise (Fig. 1). The proximity of the MELT site to the South Pacific superswell (*14*) may also give rise to lateral variations in deep-mantle thermal structure (*15*), but such temperature variations should vary approximately linearly across each OBS array. After linear trends are removed from each full set of mean delay time data, the magnitude of the variation in delays that cannot be explained by expected temperature variations is ~0.5 s for *P* waves and 2 s for *S* waves.

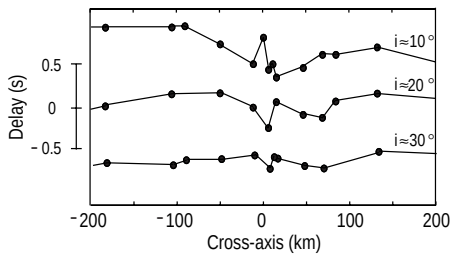

Fig. 4. Delay times of *P* waves from three events along the primary OBS array (shifted vertically for clarity). At near-vertical angles of incidence (that is, small values of the incidence angle *i*), the gradual decrease in the delays toward the rise axis is consistent with a near-vertical alignment of the crystallographic *a* axis of upper-mantle olivine crystals in an upwelling region with a half-width of about 100 km.

The lateral variations in seismic velocity structure revealed by tomographic imaging are thus dominantly caused by retained partial melt in the upper mantle beneath the rise. For melt residing in randomly oriented, film-like inclusions, the *P* and *S* velocity reduction, per percent melt, is about 1.8% and 3.3%, respectively (*16*). Given these approximations, and neglecting the possible effects of anisotropy, we can use the tomographic images to estimate relative variations in the melt fraction within about 300 km of the EPR. For squeezing depths of 300 and 600 km (see Fig. 2), the inferred variation in melt fraction is 1% or less. As the squeezing depth decreases to 150 km, the magnitude of the inferred variation in melt fraction increases to more than 1%. Additionally, the decrease in near-axis *P* and *S* wave delays between the primary and secondary OBS arrays is consistent with a decrease in the retained mantle melt concentration toward the north of as little as 0.5%. We have chosen relations among temperature, melt fraction, and velocities that would result in the smallest range in inferred melt concentrations; if anelasticity is unimportant, or if melt is primarily stored in tubules, then larger variations in melt fraction would be implied by the data (*17*).

Recent modeling studies suggest that anisotropy induced by upwelling can lead to near-axis travel-time advances that exceed the delays due to partial melt, such that *P* waves and *S* waves polarized parallel to the rise arrive early near the axis (*2*). We instead find that mean relative travel times are most delayed at the axis (Fig. 1), indicating that at this site the influence of partial melt is of greater magnitude than that of flow-induced anisotropy. A signature of upwelling-induced seismic anisotropy is evident, however, in the delay times of steeply incident *P* waves from individual events. *P* waves from three events to the west of the rise at angular distances of 146° (*PKP* phase), 86°, and 56° (Fig. 4) arrived along upper-mantle paths inclined approximately 10°, 20°, and 30° from the vertical, respectively. Except for a site located atop the axial high, the delays observed within 100 km of the EPR indicate that as the incidence angle decreases, delay times observed at near-axis OBSs become progressively early relative to sites off axis; this signal is characteristic of near-vertical alignment of the crystallographic *a* axis of upper-mantle olivine crystals beneath the spreading center (*2, 18*). The variation in delay time with incidence angle may be attributed to two causes. First, for vertical alignment of the crystallographic *a* axis of olivine, as expected for mantle upwelling, the fastest propagation direction for *P* is also vertical. Second, if the upwelling is concentrated within a relatively narrow zone beneath the axis of plate divergence, OBS stations nearer the rise record the signature of upwelling-aligned anisotropy over longer portions of the *P*-wave travel paths. By this argument, the pattern of delays observed at the steepest incidence angles (Fig. 4) is consistent with a half-width of mantle upwelling of about 100 km.

The inferred width of mantle upwelling and the lateral and vertical extent of anomalous seismic structure are consistent with melt generation or retention over a region perhaps several hundred kilometers in width. The asymmetry in velocity anomaly indicates a similar asymmetry in melt production or transport processes. Such an asymmetry may arise from the proximity of the southern EPR to the South Pacific superswell (*14*) or from asymmetric patterns of mantle upwelling and melt generation resulting from migration of the ridge relative to the lower mantle (*19*).

REFERENCES AND NOTES

1. W. R. Buck and W. Su, *Geophys. Res. Lett.* **16**, 641 (1989); D. S. Wilson, *Earth Planet. Sci. Lett.* **113**, 41 (1992); E. M. Parmentier and J. Phipps Morgan, *Nature* **348**, 325 (1990).
2. J.-M. Kendall, *Geophys. Res. Lett.* **21**, 301 (1993); D. K. Blackman *et al.*, *Geophys. J. Intl.* **127**, 415 (1996).
3. MELT Seismic Team, *Science* **280**, 1215 (1998).
4. Because of relatively high noise levels at the experiment site [S. C. Webb, *Rev. Geophys.* **36**, 105 (1998)], *P* waves could be identified only at frequencies less than 0.5 Hz on vertical-component seismometers and less than 0.14 Hz on pressure gauges. Pressure records were not used, because the time resolution is not adequate and water-column reverberations of *P* waves distort the waveforms. On the vertical component, the first reverberation arrives after the first full cycle of direct *P* and is only about one-third the amplitude, so it contributes little error to the delay time.
5. C. J. Wolfe and S. C. Solomon, *Science* **280**, 1230 (1998).
6. The azimuthal orientation of each horizontal seismometer was determined from particle motions of *P* waves and surface waves with good signal-to-noise ratios to an estimated uncertainty of 5° to 10°. The fast and slow directions for polarized shear waves were defined by the splitting analysis (*5*).
7. J. C. VanDecar and R. S. Crosson, *Bull. Seis. Soc. Am.* **80**, 150 (1990).
8. Uncertainties in the delay times (standard errors of ~100 and ~300 ms for *P* and *S* waves, respectively) were assigned visually, as the errors derived from the cross-correlation method were judged to be too small. At least one full cycle was used in the cross-correlation analysis; experiments with other time windows gave similar results.
9. B. L. N. Kennett and E. R. Engdahl, *Geophys. J. R. Astron. Soc.* **105**, 429 (1991).
10. D. R. Toomey, S. C. Solomon, G. M. Purdy, *J. Geophys. Res.* **99**, 24 (1994).
11. For three-dimensional ray tracing, a radial Earth model was defined on a grid (nodal spacing of 20 km) throughout a 600-km-deep volume centered on the rise, with cross- and along-axis dimensions of 2000 and 1200 km, respectively. The inverse problem was restricted to a two-dimensional cross-section of the

ridge. Perturbational model parameters, assigned separately from the ray-tracing model, were at horizontal and vertical nodal spacings of 20 and 25 km, respectively. The inverse problem was regularized by minimizing a stochastic penalty function and the model roughness. Results presented here were heavily smoothed (half-width of the Gaussian-shaped smoothing function was equal to the perturbational nodal spacing) and "squeezed" so that model perturbations were confined to depths less than a squeezing depth Z_s. The squeezing was implemented by assuming prior uncertainties of 10% and 0.01% in velocity above and below Z_s, respectively.

12. Synthetic data for each type of body wave were calculated for a ray set identical to that used in the inversion of actual data. Gaussian noise with a standard deviation of 0.1 s and 0.3 s was added to the synthetic *P* and *S* wave data, respectively.
13. S. Karato, *Geophys. Res. Lett.* **20**, 1623 (1993).
14. M. K. McNutt and A. V. Judge, *Science* **248**, 969 (1990).
15. J. R. Cochran, *Geophys. J. R. Astron. Soc.* **87**, 421 (1986); M. A. Eberle, D. W. Forsyth, E. M. Parmentier, *J. Geophys. Res.*, in press.
16. H. Schmeling, *Phys. Earth Planet. Inter.* **41**, 34 (1985); U. H. Faul, D. R. Toomey, H. S. Waff, *Geophys. Res. Lett.* **21**, 29 (1994).
17. D. W. Forsyth, in *Mantle Flow and Melt Generation at Mid-Ocean Ridges,* J. Phipps Morgan, D. K. Blackman, J. M. Sinton, Eds., vol. 71 of *Geophysical Monograph Series* (American Geophysical Union, Washington, DC, 1992), p. 1.
18. D. K. Blackman, J. A. Orcutt, D. W. Forsyth, J.-M. Kendall, *Nature* **366**, 675 (1993).
19. S. Stein, H. J. Melosh, J. B. Minster, *Earth Planet. Sci. Lett.* **36**, 51 (1977); H. Schouten, H. J. B. Dick, K. D. Klitgord, *Nature* **326**, 835 (1987).

20. D. W. Forsyth and C. J. Wolfe provided helpful comments. Supported by the Ocean Sciences Division of NSF.

12 February 1998; accepted 21 April 1998

Structure of the Upper Mantle Under the EPR from Waveform Inversion of Regional Events

Spahr C. Webb* and Donald W. Forsyth

Waveform inversions of seismograms recorded at the Mantle Electromagnetic and Tomography (MELT) Experiment ocean bottom seismometer array from regional events with paths following the East Pacific Rise (EPR) require that low shear velocities (<3.7 km/s) extend to depths of more than 100 km below the rise axis. Velocities increase with average crustal age along ray paths. The reconciliation of Love and Rayleigh wave data requires that shear flow has aligned melt pockets or olivine crystals, creating an anisotropic uppermost mantle.

Earthquakes on transform faults along the EPR during the 6-month-long deployment of ocean bottom seismometers (OBSs) of the MELT Experiment provided ray paths that closely follow the ridge crest and allowed direct observation of near-axis, upper mantle structure (Fig. 1). Previous models of ridge crest upper mantle structure (*1*–*3*) derived with surface wave observations from land have been limited in horizontal resolution to scales of 1000 km or more (*4*).

Three transform earthquakes on the EPR provided good records at the ocean bottom array (Fig. 1). Noise levels varied substantially across the array, reflecting differences among instruments and between sites. We selected a subset of the MELT array waveforms with good signal-to-noise ratios (SNRs) for each event (*5*). Horizontal component noise levels were higher and more variable than vertical noise levels because of current-induced tilt noise, but good-quality horizontal records were obtained on a small subset of the array (Fig. 2).

The vertical waveforms include both Rayleigh surface waves and *S* phases that are polarized with a radial and vertical component (SV). These waves were also recorded on the radial component of horizontal motion, but we used only the vertical component because the SNR was better. Rayleigh wave velocities depend on density and both compressional and shear velocity, but the primary sensitivity is equivalent to that of a vertically polarized, horizontal traveling *S* wave (*6*). Love surface waves and the horizontal (SH) component of *S* phases are polarized so that they are transverse to the direction of propagation and can be detected only on the noisier, horizontal components (*5*).

Wave speeds in mantle rocks are anisotropic; shear and compressional wave velocities depend on the direction of travel, and shear wave velocities depend on the sense of polarization. The effects of weak anisotropy result in an apparently different model for shear wave velocities for the Love wave measurements than for the Rayleigh wave observations. The ratio of the shear velocities in the two models provides an estimate of the anisotropic component, although in strongly anisotropic material, Love and Rayleigh wave data are better modeled as coupled modes (*7*, *8*).

We fit the observed waveforms to synthetic seismograms calculated for laterally homogeneous models with a reflectivity code (*9*) modified by the incorporation of the instrument responses into the code. We applied a bandpass filter (0.008 to 0.06 Hz) to suppress the long-period noise and the short-period Rayleigh waves strongly affected by multipathing and horizontal refraction (*10*). The OBS instrument response in this band is proportional to acceleration (*11*). Models were iteratively modified to best fit the data with the use linear inverse

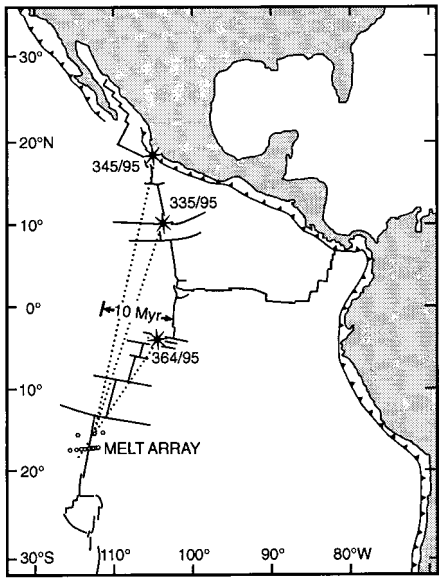

Fig. 1. Location of the three regional events along the EPR and the MELT Experiment OBSs used in this study. Approximate ray paths are shown.

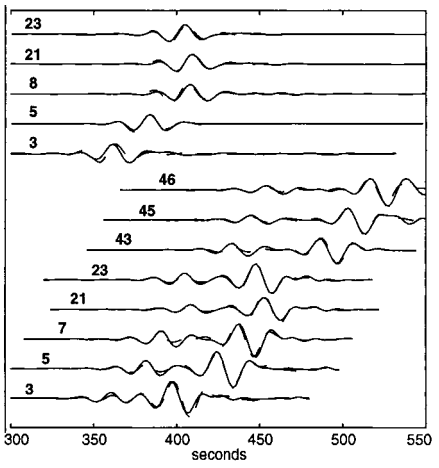

Fig. 2. Love wave (tangential component, top five traces) records and Rayleigh wave (vertical component, bottom eight traces) records for the 364/95 event, with synthetic seismogram fits based on the models shown in Fig. 3. Site number is shown for each trace.

S. C. Webb, Scripps Institution of Oceanography, University of California, San Diego, La Jolla, CA 92093, USA. D. W. Forsyth, Department of Geological Science, Brown University, Providence, RI 02912, USA.

*To whom correspondence should be addressed at scwebb@ucsd.edu